DROP-IT

DELIVERABLE 5.1

ASE in inkjet-printed B- LFP-based waveguides on flexible substrates

Due date of deliverable: 2021/10/31

Actual submission date: 2021/11/30

Deliverable number:	D5.1
Due date:	30.10.2021
Nature[1]:	R
Dissemination Level[1]:	PU
Work Package:	WP5
Lead Beneficiary:	UVEG
Contributing Beneficiaries:	UJI, UB

[1] **Nature:** R = Report, P = Prototype, D = Demonstrator, O = Other
Dissemination level PU = Public PP = Restricted to other programme participants (including the Commission Services) RE = Restricted to a group specified by the consortium (including the Commission Services) CO = Confidential, only for members of the consortium (including the Commission Services) Restraint UE = Classified with the classification level "Restraint UE" according to Commission Decision 2001/844 and amendments Confidential UE = Classified with the mention of the classification level "Confidential UE" according to Commission Decision 2001/844 and amendments Secret UE = Classified with the mention of the classification level "Secret UE" according to Commission Decision 2001/844 and amendments

This project has received funding from the European Union's Horizon 2020 research and innovation programme under **Grant Agreement No. 862656**.

DOCUMENT HISTORY

Version	***Date***	***Reason of change***
1	2021/11/10	UVEG contribution
2	2021/11/29	UVEG and UB revisions
3	2021/11/30	UVEG revision
4	2021/11/30	UB revision

This project has received funding from the European Union's Horizon 2020 research and innovation programme under **Grant Agreement No. 862656**.

Table of Content

This project has received funding from the European Union's Horizon 2020 research and innovation programme under **Grant Agreement No. 862656**.

1 Introduction

This deliverable reports the results of Amplified Spontaneous Emission (ASE) on waveguides containing lead-free perovskites (LFP) thin films fabricated on flexible substrates. Among the different LFP materials studied during the project (see Annex I), polycrystalline thin films of $[HC(NH_2)_2]SnI_3$ (abbreviated here as $FASnI_3$) presented the strongest PL emission intensity together with the ~ 1 ns lifetime of the $FASnI_3$, which are suitable parameters for stimulated emission. Indeed, these films illuminated under nanosecond excitation (Nd:Yag laser doubled at 532 nm and tripled to 355 nm, 1 ns, 1 kHz) demonstrated the generation of ASE by back-scattering (both excitations) and waveguide geometry (excitation at 532 nm). In the present report, we summarize our result comprising: (i) the fabrication of high-quality thin films. (ii) the demonstration of ASE, (iii) the demonstration of random lasing as the basis for next deliverables.

2 Description of work & main achievements

2.1 Fabrication of tin-based films for optical amplification and lasing.

The first goal of the experimental work was the fabrication of high-quality $FASnI_3$ layers in the with the waveguide architecture shown in figure 1. In a first approach, the LFP thin film were deposited on a rigid SiO_2 (2 mm)/Si substrate (figure 1a), and once the fabrication process was properly optimized, the $FASnI_3$ was incorporated on a Polyethylene terephthalate (PET) flexible substrate (figure 1b). In both cases, the LFP was covered by a cladding of Poly(methyl methacrylate) (PMMA) with two purposes: (i) the PMMA acts as a protective layer for the semiconductor against air moisture, (ii) the transparency of the polymer enables the propagation of the excitation beam through high order cladding modes. Thicknesses of the $FASnI_3$ and PMMA were fixed to 0.8 µm and 0.2 µm, respectively.

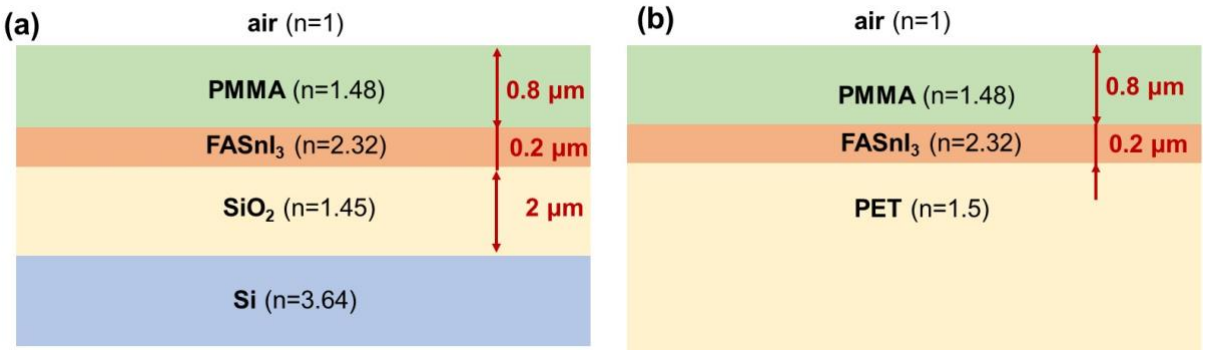

Figure 1. Architecture of the waveguide geometries chosen to demonstrate ASE. (a) 200 nm $FASnI_3$ deposited on rigid SiO_2 (2 µm)/Si. (b) 200 nm $FASnI_3$ deposited on flexible PET. All samples were covered by a 800 nm PMMA cladding layer.

2.1.1 Thin film deposition by spincoating

Tin (II) iodide (SnI_2, 99.99%), tin(II) fluoride (SnF_2, 99%), N,N-dimethylformamide (DMF, 99.8%) and dimethylsulfoxide (DMSO, 99.8%) were purchased from sigma-aldrich. Formamidinium iodide (FAI. 99.99%) was purchased from Greatcell Solar Materials. These materials were used as received with no further purifications. Dipropylammonium iodide salt was synthesized with the following procedure:

10 g Dipropylamine was added to 30 mL of cold EtOH, then 13 mL of HI was added dropwise to the flask under vigorous stirring and the white solid formed after the addition of HI was filtered and washed with 100 mL of cold diethylether and it was recrystallized using EtOH. To prepare the $FASnI_3$ precursor solution, 298 mg of SnI_2 (0.8M), 123.8 mg of FAI (0.72M), 36.65 mg of DipI (0.16 M), 1.9 mg of $NaBH_4$ (0.05 M) and 12.48 mg of SnF_2(0.08 M) were dissolved in 1 ml of a mix solution of DMSO:DMF (9:1, v/v) and stirred over night at room temperature, following literature. [cite] After the fabrication process, a 3-day light soaking treatment was made inside a N_2 filled glovebox, using an LED lamp. This is the same procedure used for the fabrication of stable solar cells by spicoating (see Deliverable 3.2).

The different substrates (SiO_2/Si or PET) were washed with ethanol, acetone and isopropanol, respectively in a ultrasonic bath for 5 minutes each. After the wash, the substrates were dried with N_2 flux, and right before the perovskite film, they were treated in UV-Ozone for 20 min. The perovskite film was deposited by one step antisolvent method, by adding $FASnI_3$ precursor solution, on top of the appropriate substrates and spin coated at 4000 rpm for 50 s. Then 400 µl of Chlorobenzene was drop on top of the substrate after 20s of spinning, followed by an annealing at 70 ºC and 100 ºC for 1 min and 19 min, respectively. Fabricated films presented good homogeneity and gran sizes of around 1 µm, see SEM images in figure 2.

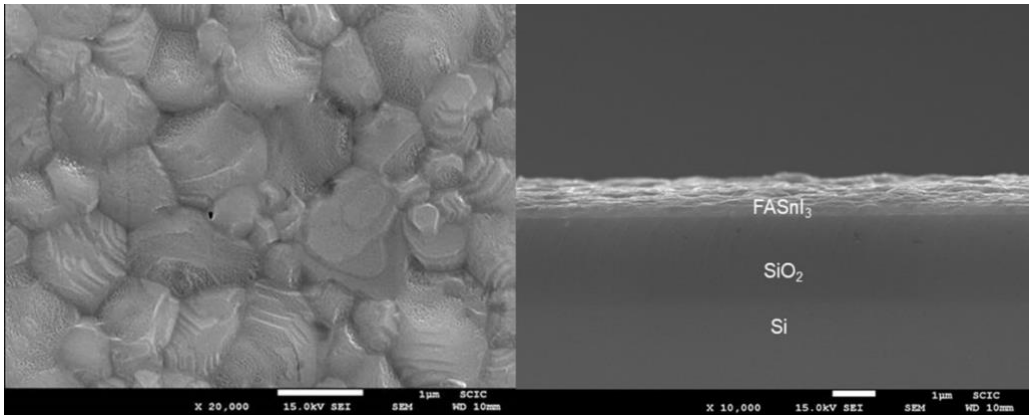

Figure 2. SEM images of the PMMA/$FASnI_3$ waveguide deposited on the SiO_2/Si substrate (left: top view, right: cross section).

2.1.2 Thin film deposition by inkjet printing

The precursor inks were prepared using commercially available precursors (DMSO and DMF) inside a nitrogen filled glovebox with well controlled oxygen and humidity levels below 1 ppm. The recipe for the $FASnI_3$ composition presented in D2.3 and D2.4 was modified to meet the inkjet printing requirements. In particular, it was important to reduce the concentration of the precursor ink and a solvent ratio (DMSO:DMF, 4:1) to enable inkjet printing and achieve a submicron thick films. The colloidal solution of $FASnI_3$ in DMSO:DMF (4:1), as received from our partner SAULE, was diluted into DMSO:DMF. After that, the obtained solutions were stirred and finally we collect the supernatant. All the materials were inkjet printed on flexible substrates using Dimatix Materials Printer DMP-2850 equipment located and operated inside a glovebox in inert conditions. A square pattern of 1 cm^2 is inkjet printed with different thicknesses. The optimization of the printing process for each ink solution requires of two main steps:

1) Samples were inkjet printed with different drop spacing in the range of 20 µm to 50 µm to carry out the best value that promote the complete uniform thin layer without pinholes. The optimized drop spacing allow controlling the minimum thickness and obtaining the lowest roughness of the thin film. By printing several steps to reach the expected thickness the amount of solution of the layer is subsequently kept on the platen printer (pre-annealing) in the range of 30 °C to 60 °C.

2) After receiving a stable, dry layer with the expected colour for each material, samples were annealed at 110 °C for 10 minutes in a mini hot vacuum hotplate into the glovebox. The pre-annealing step is applied during the printing process to avoid local de-wetting of the precursor ink.

2.1.3 Device assembly

Once the $FASnI_3$ thin films were deposited on the appropriate substrate, a PMMA solution (100mg/1ml CB) was spin coated on top of the perovskite film at 3000 rpm for 30s and annealed at 70 ºC for 1 minute and 4 minutes at 100 ºC. Finally, samples were cleaved for end-fire coupling purposes.

2.2 Characterization of optical amplification and lasing under back scattering.

As a first study to obtain information about material gain and limitations, the photoluminescence (PL) of $FASnI_3$ thin films was characterized at cryogenic temperature (20 K) in the back-scattering geometry (see Figure 3a) under sufficiently high laser pumping: the surface of the films was illuminated with a Nd:Yag laser (1 ns, 1 kHz) doubled at 532 nm. The backscattered PL signal was collected by an appropriate lens, dispersed by a double 0.3 m focal length grating spectrograph and detected with an Andor Newton 970 EMCCD camera.

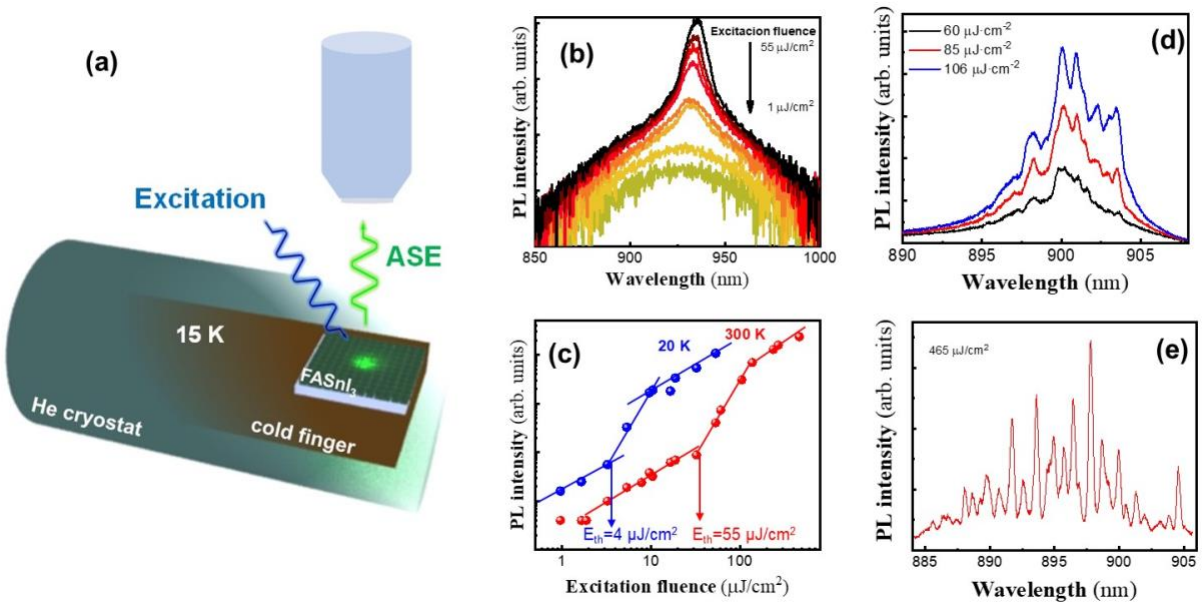

Figure 3. Characterization of ASE measured in $FASnI_3$ thin films under back-scattering geometry. (a) Experimental set-up. (b) PL spectra for different excitation fluences collapses into a narrow line above 4 µJ/cm² at temperatures from 20 K to 300 K. (c) PL intensity as a function of the excitation fluence in a log-log plot. Blue and red symbols refer to T=20 K and T=300 K, respectively. (d) The PL spectra at 20 K show narrow peaks that could be attributed to random lasing (RL) resonances. (e) RL peaks measured on similar $FASnI_3$ thin films deposited on flexible PET.

2.2.1 Rigid substrates

Here the samples consisted of $FASnI_3$ thin films deposited on a glass substrate and capped with a thin layer of PMMA to protect against degradation. Excitation fluence (I) was ranged between 1 and 500 µJ/cm^2 with neutral density filters. At 20 K, for I < 4 µJ/cm^2 the PL shows a Gaussian shape centered at 925 nm with a full width at half maximum (FWHM) of around FWHM = 55 nm. Nevertheless, above a certain threshold of around I = 4 µJ/cm^2 the spectrum collapses to a narrow peak (blue symbols in Figure 3b), which is a clear signature of stimulated emission. In particular, the FWHM decreases progressively down to FWHM = 9 nm at the highest excitation fluence (I = 55 µJ/cm^2). The narrowing of the PL spectrum is accompanied by a superlinear increase of the PL intensity (I_{PL}) as a function of I above this threshold (see blue symbols in Figure 3c), which corroborates the generation of optical gain. Moreover, the log-log plot of Figure 3 c shows an S curve with three different regions: for I < 4 µJ/cm^2 the PL is generated by spontaneous recombination and the I_{PL} follows a linear law with I ($I_{PL} \propto I$), between the range 4 µJ/cm^2 < I < 10 µJ/cm^2 I_{PL} grows superlinearly with I due to the generation of stimulated emission, above I > 10 µJ/cm^2 I_{PL} presents again a linear regime. This last region of the curve occurs when all excited states are filled, and it is characteristic of cavity lasing action. It is worth mentioning that experiments carried out at different temperatures show a similar S-shape with the shift of the threshold characteristic for semiconductor materials. At room T (red symbols in Figure 3c) stimulated emission was maintained with a threshold of 55 µJ/cm^2. A more careful analysis of the PL spectra above the threshold shows a set of narrow peaks (<1 nm) whose spectral position remains unchanged with the excitation fluence and the time (see Figure 3d). These spikes are attributed to strongly localized random lasing (RL) lines generated by self-formed paths in the semiconductor thin film (more experiments are being developed to define more precisely the physical origin, but phenomenologically we would ascribe to RL). It is worth mentioning that we obtained a full wave of half maximum FWHM ≈ 0.1 nm for the narrowest lines, that corresponds to the quality factor as high as Q ≈ 10^4. At room temperature, broader RL lines are usually observed, but in some cases sufficiently narrow lines with FWHM ≈ 0.2 nm were detected that corresponds to a quality factor Q ≈ $0.45 \cdot 10^4$.

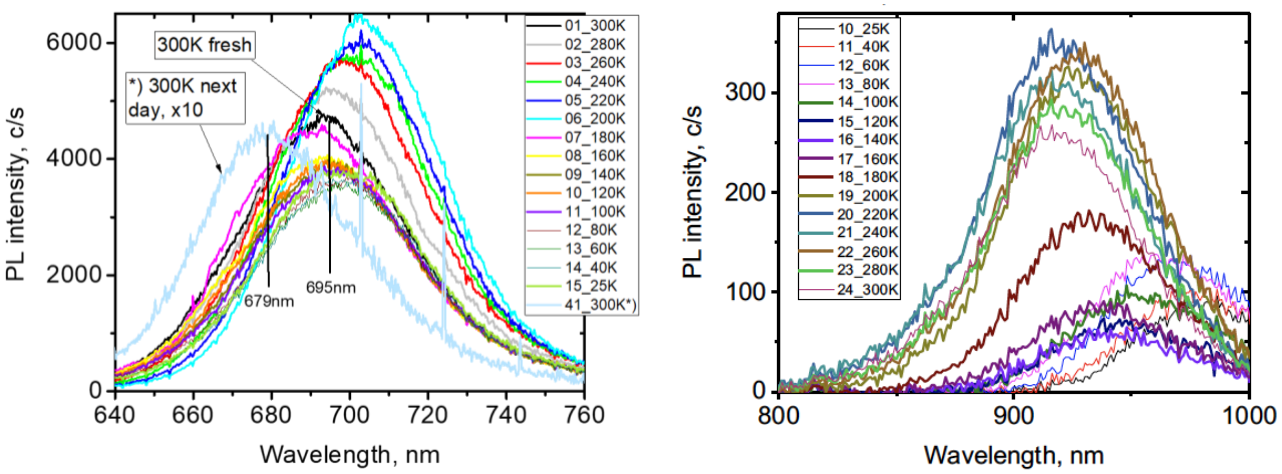

Figure 4. PL spectra as a function of temperature in films of $CsSnBr_3$ and $CsSnI_3$ nanocrystals (synthesized by the hot injection method) deposited by drop-casting on Si-SiO2 substrates. The excitation was made by a pulsed Ti:sapphire laser double to 406 nm.

Films of $CsSnBr_3$ and $CsSnI_3$ nanocrystals were also studied both on rigid (Figure 4) and flexible substrates (not shown). More information on these nanocrystals can be found in the 2nd-year report for WP1. These nanomaterials seem promising, but further investigations are needed in the future

to improve the preparation of samples to avoid the negative effect of ambient conditions, because they do not exhibit ASE at the moment.

2.2.2 Flexible substrates

$FASnI_3$ films fabricated on flexible substrates show similar ASE/RL result with higher threshold, ASE was observed above 25 µJ/cm^2. Figure 3e presents the RL spectra measured on $FASnI_3$ thin films deposited on a flexible PET substrate at 15K and excited at 460 µJ/cm^2. Despite the higher threshold, the RL spikes also consists of 1 nm narrow lines with good stability in time. For waveguides based in inkjet-printed $FASnI_3$ films the material has similar optical quality than those deposited by spin-coating and ASE is also observed, as shown below.

At these conditions, we conclude that $FASnI_3$ thin films pumped at ns excitation demonstrate stimulated emission and lasing action, even at room T. The results can be reproduced from rigid to flexible substrates, indicating that the material under study accomplishes the requirements to succeed in the present task of DROP-IT.

2.3 Characterization of optical amplification and lasing under waveguide geometry.

Once the generation of ASE (and RL) with $FASnI_3$ films was demonstrated in back-scattering geometry, the next step was to measure the stimulated emission in an optical waveguide geometry. For this purpose, we chose the design shown in Fig. 1 that we successfully applied with lead-based perovskites. This architecture consists of a thin PMMA/$FASnI_3$ bilayer structure deposited on the appropriate substrate, rigid SiO_2 (2 µm)/Si or flexible PET, as illustrated in figure 1. This configuration provides an efficient excitation of the active media together with a strong light-matter interaction for the emitted PL and allows the copropagation of the the PL and the pump beams along the entire length of the structure (≈1 mm). Waveguides were characterized by end-fire coupling a Nd:YAG laser doubled to 532 nm (1 ns pulse, 1 kHz) at the input edge of the sample with the aid of a 40× microscope objective, and collecting the waveguided PL at the output edge of the sample with a 20× microscope objective (see figure 5). All measurements in the waveguide geometry were carried out at room temperature and ambient conditions, and that the sample was not protected with encapsulation, see scheme in figure 5.

2.3.1 Design of the waveguide

The design of the WG is based on the refractive-index contrast (Δn) between the different materials and the engineering of the propagating modes with the geometrical parameters. For this purpose, propagating modes confined in the WG were calculated with a multilayer algorithm. Table 1 presents the effective refractive indexes at 532 nm (pump) and 890 nm (PL) in the rigid (SiO_2/Si) and flexible (PET) substrates. The thickness of the $FASnI_3$ (d_1) is fixed to d_1=200 nm to assure single mode propagation at the PL wavelength (890 nm) in both transverse electric (TE) and transverse magnetic (TM) polarizations. Red line in the inset of Fig. 5 shows the power distribution of the TE_0 mode (TM polarization present a similar behavior). This mode is highly confined in the semiconductor with more than 80% of the electric field distribution concentrated in this layer, see red line in the inset. On the other hand, the thickness of the PMMA (d_2) is fixed between 600-1000 nm to allow the propagation of the TE_2 (TM_2) cladding mode at the pump wavelength (532 nm), whose power distribution is mainly confined in the polymer (green line). This TE_2 (TM_2) mode is characterization by its low attenuation, derived from the absence of losses in the PMMA, and the overlap of the evanescent field with the active region (0.2 % of the mode). Then, it represents a suitable mechanism to pump the entire length of the WG (1 mm) by injecting the excitation beam at the input edge of the structure. The introduction of a rigid substrate only results in a slight modification of the propagating modes and their effective refractive indexes.

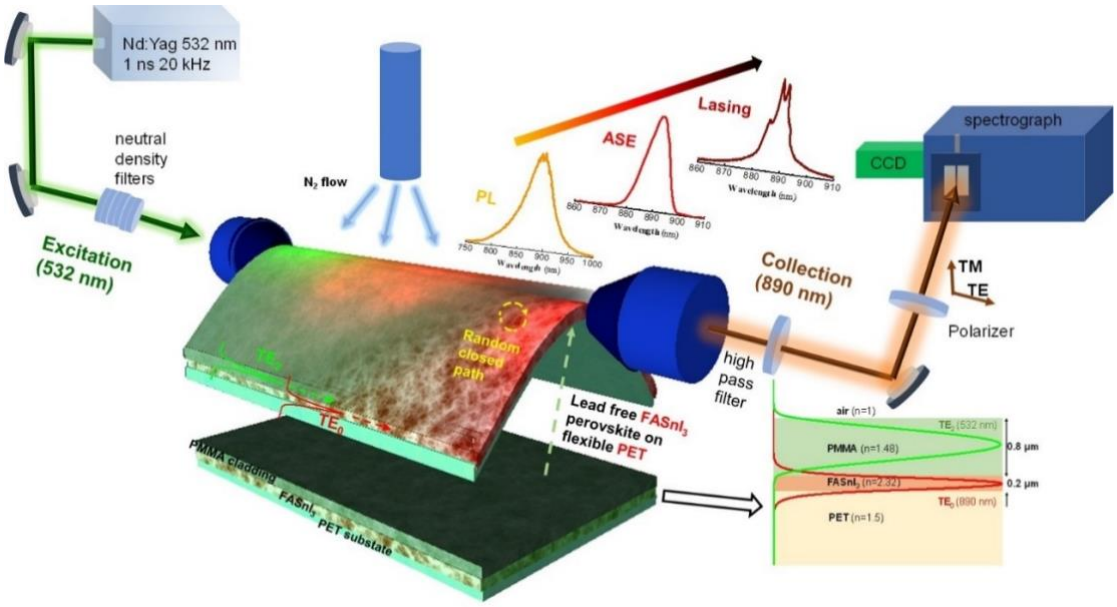

Figure 5. Scheme of the sample structure and the experimental setup.

Mode	532 nm	890 nm
TE_0	2.27559-0.732i (2.27489-0.734i)	2.05021-0.0138i (2.04207-0.014i)
TE_1	1.6254-0.743i (1.624-0.757i)	-
TE_2	1.46201-0.0023i (1.46205-0.0022i)	-

Table 1. Effective refractive indexes of the WG fabricated in PET substrates. In parenthesis the effective refractive index of the WG fabricated on rigid substrates.

2.3.2 Summary of results.

The PL decoupled from the output edge of the waveguide showed the generation of ASE above excitation fluences of 0.1 and 1.5 μJ/cm^2 in rigid and flexible substrates, respectively. The waveguide devices also show narrow lasing lines (<1 nm), again attributed to RL, in comparison to previous results in backscattering geometry. These figures of merit improve the results obtained in previous RL systems fabricated on either lead or lead-free perovskite morphologies. More interestingly, the RL shows a preferable transverse electric (TE) polarization, which enables practical applications where the control of the polarization becomes necessary. The RL action is also studied under bending conditions in the flexible device to stablish the dependence of the threshold, PL intensity and dichroism with the curvature radius.

3 Results

3.1 $FASnI_3$ waveguides fabricated on rigid substrates..

3.1.1 Generation of ASE and RL

The waveguided PL spectrum decoupled from the waveguide fabricated on the rigid SiO_2/Si substrate, see figure 6a, demonstrates the waveguiding of the fundamental TE_0 mode at the PL wavelength, see figure 6b. The PL spectra shows a progressive narrowing by increasing the excitation fluence (*I*) due to the generation of ASE after a certain threshold, see Fig. 6c. Moreover, for large laser excitation, the ASE spectrum exhibits sharp peaks, which is a distinctive feature of RL. The log-log plot of the waveguide PL intensity (I_{PL}) as a function of fluence *I* shows the typical S-shaped curved characteristic of lasing action (hollow brown circles in Fig. 6d), in parallel to the progressive reduction of the full wave at half maximum (FWHM) of the signal spectrum above the ASE threshold (hollow blue circles in Fig. 6e). The analysis of the spectrum of waveguided emitted light as a function of *I* reveals four different regions indicated by vertical dashed lines in Fig. 6d. For $I < 100$ nJ/cm^2 the PL spectrum is characterized by a Gaussian shape centered at 890 nm with a FWHM ≈ 100 meV (64 nm), hence corresponding to the spontaneous emission of $FASnI_3$ due to exciton recombination and exhibiting a linear variation with fluence $I_{PL} \propto I$. Above a threshold of around $I \approx 100$ nJ/cm^2, the spectrum of waveguided emitted light progressively collapses down to a narrow line of 10 meV (6.4 nm) that shows a superlinear increase ($I_{PL} \propto I^{3.2}$). This behaviour is a clear signature of stimulated light emission and indicates the suitability of the proposed material for optical amplification. For $I > 300$ nJ/cm^2, I_{PL} shows again a linear growth with the excitation ($I_{PL} \propto I$), where the already narrow ASE line contains narrower spikes attributed to the RL action. For $I > 2$ µJ/cm^2 I_{PL} saturates and the ASE line FWHM exhibits a slight broadening from 10 to 15 meV. The variation of the emission intensity with laser fluence can be nicely reproduced with a standard semiconductor laser model (solid brown line in Fig. 6d).

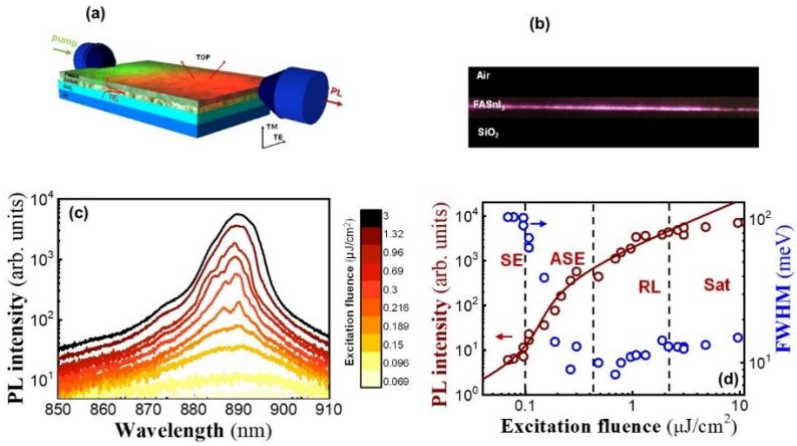

Figure 6. ASE and RL on $FASnI_3$ rigid waveguide. (a) Scheme of the sample (b) CCD image of waveguided emitted light registered at the leaving face of the waveguide (c) PL spectra for different excitation fluences. (d) PL intensity (brown and left axis) and FWHM (blue and right axis) as a function of the excitation fluence. Brown solid line corresponds to the modelling with a standard laser equation.

Finally, the analysis of the narrow RL lines on different positions, see figure 7, indicates linewidths of RL lines ranged between 1 and 2 meV (0.6-1.2 nm), ten times narrower than the ASE linewidth, which means Q ≈ 700 - 1400.

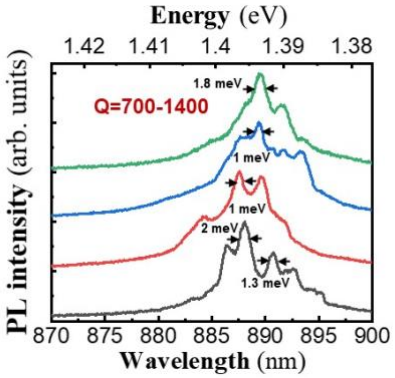

Figure 7. RL emission collected at the output edge of different samples.

3.1.2 Directionality and polarized emission

The strong localization of RL modes demonstrated in previous section represents the origin of the observed high Q factor and their stability. Nevertheless, our device presents additional advantages derived from the propagation of light along the WG and the important light confinement in the semiconductor film allowed by the structure. Although the emitted light produced by exciton recombination is initially omnidirectional, the WG configuration selects a preferable momentum for the emitted light parallel to the TE_0 (TM_0) mode. Figure 8 compares the RL light collected in TE (blue), TM (red) and TOP (black) directions, see experimental configurations in figure 8a-b. Despite that the three collection conditions show similar spectrum, figure 8c-d, and threshold, see figure 8e, the outcoupled emitted light is much more intense in the WG direction. In particular, the emission of the film shows a preferent TE polarization in the three regimes: spontaneous emission, ASE and RL (figure 8e-f), even if seems more important the TE polarization for the ASE-RL regime. In the spontaneous emission the ratio $I_{TE}/I_{TM} \approx 3.5$, while it grows above the ASE/RL thresholds. At these conditions, the light collected from the TE_0 mode exhibits 1-fold higher intensity than the TM counterpart (figure 8f).

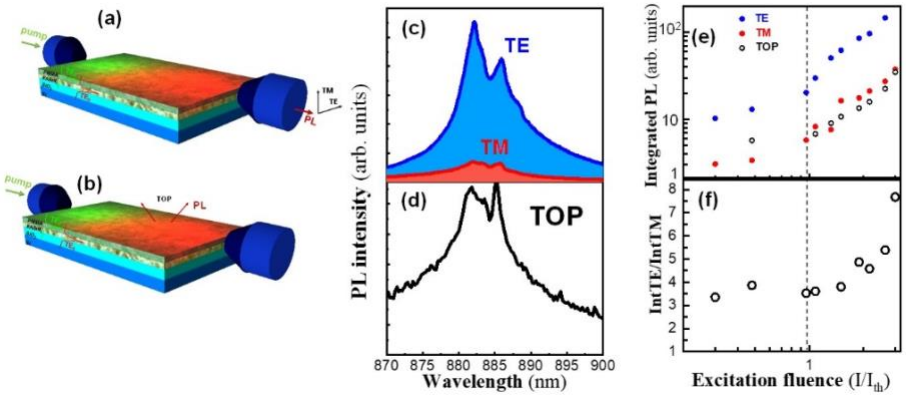

Figure 8. Experimental configuration to measure: (a) Waveguided TE/TM PL, (b) TOP emitted PL. RL spectra collected in (c) TE/TM polarization, (d) surface of the sample (TOP). (e) Integrated PL intensity. Blue, red and open symbols correspond to TE, TM and TOP respectively. (f) Ratio of the integrated intensities in TE and TM polarizations as a function of I.

3.1.3 Evolution of RL with time.

Figure 9 shows the evolution of the RL spectra as a function of time. From t=0 (figure 9a) to t=1500 s (figure 9b) the spectra only show small changes in the linewidth, while the average PL intensity remains constant, see figures 9c-d.

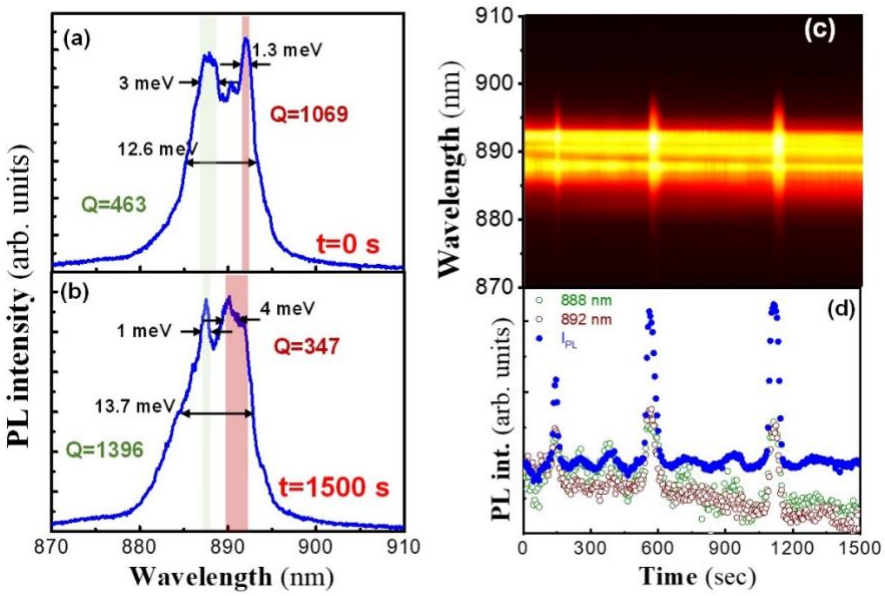

Figure 9. Evolution of the RL action during time in a rigid substrate. (a) Spectra at t=0. (b) Spectra at t=1500 s. (c) MAP of the PL spectra as a function of the time. (d) Evolution of the PL intensity (I_{PL}) and RL lines at 888 nm (green symbols) and 892 nm (brown symbols).

3.2 $FASnI_3$ waveguides fabricated on flexible substrates.

Finally, we have succeeded in the demonstration of ASE/RL on a flexible waveguide, particularly a PET substrate, one of the most used in the market for many applications. This success is one of the goals of DROP-IT and indicates the potential benefits of the developed technology.

3.2.1 ASE spectra.

Our flexible waveguides also allow the propagation of the excitation beam at 532 nm though the TE_2 mode and the propagation of TE_0 (TM_0) mode at 890 nm and its decoupling at its output edge, as shown in the image of figure 10a, again due to the high spatial confinement in the lead-free perovskite thin film. ASE and narrow RL lines are also observed by increasing sufficiently the excitation fluence, as shown in figure 10b. The evolution of I_{PL} and FWHM of outcoupled spectra with the excitation laser fluence is shown in figure 10c (brown and blue solid circles). The threshold derived from the superlinear increase of I_{PL} and the narrowing of the FWHM is in the range 1.5 - 3 $\mu J/cm^2$, which is one order of magnitude higher than that found for the best benchmark devices in Si/SiO_2, but remarkably lower than the threshold obtained in other systems. Again, the experimental data shown in figure 6c can be nicely fitted with the standard Rate-Equation model. So, our flexible waveguide presents similar gain and RL features in rigid and flexible substrates.

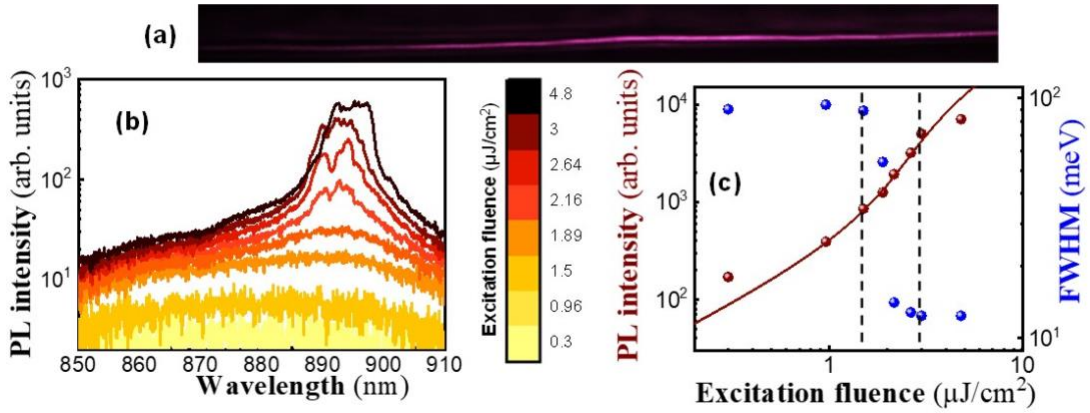

Figure 10. ASE and RL on $FASnI_3$ a flexible waveguide. (a) TE_0 at 890 nm collected at the output edge of the WG. (b) PL spectra for different excitation fluences. (c) PL intensity (solid brown circles) and FWHM (solid blue circles) as a function of the excitation fluence. Brown solid line corresponds to the modelling with a standard laser equation.

Finally, our flexible WGs still provides good directionality of the RL modes and a strong dichroism of emitted light, with 86% of the total I_{PL} in TE polarization, as shown in figure 11.

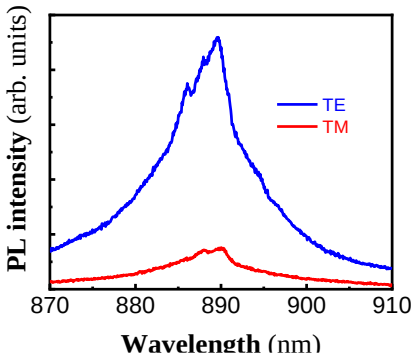

Figure 11**.** PL decoupled at the output edge of the PET flexible substrate in TE (blue) and TM (red) polarization. There is a strong dichroism with 86 % of the total PL intensity in TE.

3.2.2 Evolution of RL with time.

The time evolution of the waveguided emitted light spectra under operational conditions in ambient atmosphere (with N_2 flowing on top of the WG) indicates a good stability of the RL lines, because only small changes are observed in the linewidth from t = 0 to t = 1500 s, see figures 12a-b. In agreement, the integrated intensity remains practically constant after t = 300s.

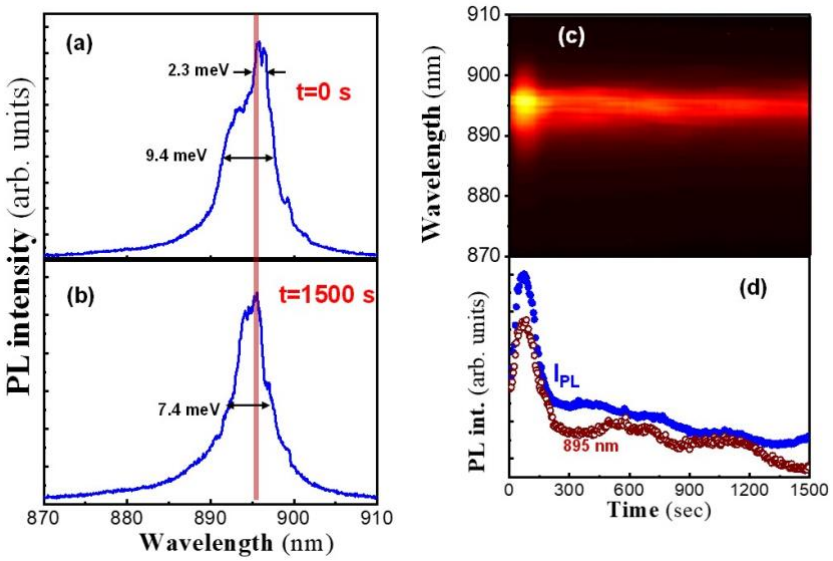

Figure 12. Evolution of the RL action during the time in a flexible substrate. (a) Spectra at t=0. (b) Spectra at t=1500 s. (c) MAP of the PL spectra as a function of the time. (d) Evolution of the PL intensity (I_{PL}) and RL lines at 888 nm (green symbols) and 892 nm (brown symbols).

3.2.3 Operation of the waveguide devices under bending.

Finally, it is important to analyze the ASE/RL emission as a function of the curvature of the substrate, *c*, in order to stablish the limits of the flexible device under practical operation. The scheme of figure 13a illustrates the experimental set-up on a curved substrate. In particular, we compared the performances of flat substrate (*c=0*) with four bending radius *ρ = 0.2, 0.4, 0.5 and 0.7 cm* corresponding to curvatures *c = 1.4, 2, 2.5 and 5 cm*$^{-1}$. The emission spectra above threshold (> 2 μJ/cm^2) for the different curvatures are plotted in figures 13b and 13c for TE and TM polarizations, respectively. For flat substrates or small bends (*c = 1.4 mm*$^{-1}$) the PL consists of an ASE band centered at 890 nm with a FWHM ≈ 10 nm and containing the narrow RL spikes. For higher bending curvatures (c = 2-5 mm^{-1}), however, the ASE band broadens, RL is not observed (at measured excitation fluences) and shows a progressive blueshift. The log-log plots of figure 13d compare I_{PL} and FWHM of the outcoupled waveguided emitted light as a function of fluence for the flat substrate and four bending conditions. Clearly, the threshold (I_{th}), indicated in the figures with a dashed line, increases with the curvature from 1 μJ/cm^2 (*c=0*) to 10 μJ/cm^2 (*c=2.5 mm*$^{-1}$). For *c= 5 mm*$^{-1}$ the I_{PL} intensity does not show a clear transition between a linear and superlinear increase, and we believe that the saturation condition due to heating is reached at such a high excitation fluence and hence it would represent a limit for ASE (without additional heat dissipation measures). The dependence of I_{th} with *c* shows a progressive increase that can be empirically fitted by $I_{th}=1-0.87\cdot c+1.79\cdot c^2$ (figures 13e), where I_{th} and *c* are given in μJ/cm^2 and mm^{-1}, respectively. In agreement, the variation of the narrower *FWHM* with *c*, see figure 13f, indicates a progressive broadening of the spectra following the phenomenological law $FWHM=10.7-0.98\cdot c+1.55\cdot c^2$, where *FWHM* and *c* are given in nm and mm^{-1}, respectively. More importantly the analysis of the ratio between the TE and TM intensities (I_{TE}/I_{TM}) indicates that the dichroism decreases with the curvature from I_{TE}/I_{TM} =4.8 (*c=0*) to 10 $I_{TE}/I_{TM}=2.7$ (*c=2.5 mm*$^{-1}$). In particular, our experimental data suggests that I_{TE}/I_{TM}) can be controlled with c through the law $I_{TE}/I_{TM}=2.6+2.2\cdot e^{-c/1.21}$, see figure 13g. Finally, it is worth mentioning that the bending effects were reversible during the duration of the experiment.

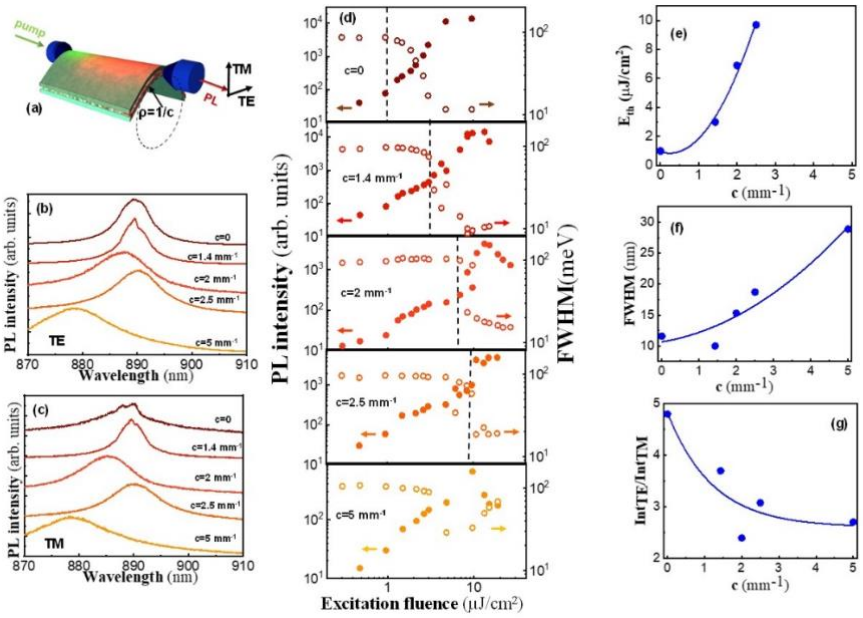

Figure 13. Analysis of the ASE/RL performances with the curvature. (a) scheme of the excitation/collection under bending. PL spectra above threshold with different curvatures: (b) TE, (c) TM. (d) Log-log plot of the I_{PL} (closed symbols) and FWHM (open symbols) as a function of I for TE polarization and the different curvatures. Dependence of the figures of merit with the curvature: (e) Threshold, (f) FWHM, (g) Ratio of TE/TM intensities.

3.3 $FASnI_3$ waveguides fabricated on flexible substrates by ink-jet printing.

In the last step of the present deliverable and after being optimized the deposition of lead-free perovskites by inkjet printing in glove box, the waveguide structure proposed in Figure 1 was also fabricated by ink-jet printing on the corresponding flexible substrate. Figure 14 shows a photograph of the ink-jet printed device. This printing technology allows the deposition of layers with good homogeneity and the possibility to grow patterns with different sizes and shapes.

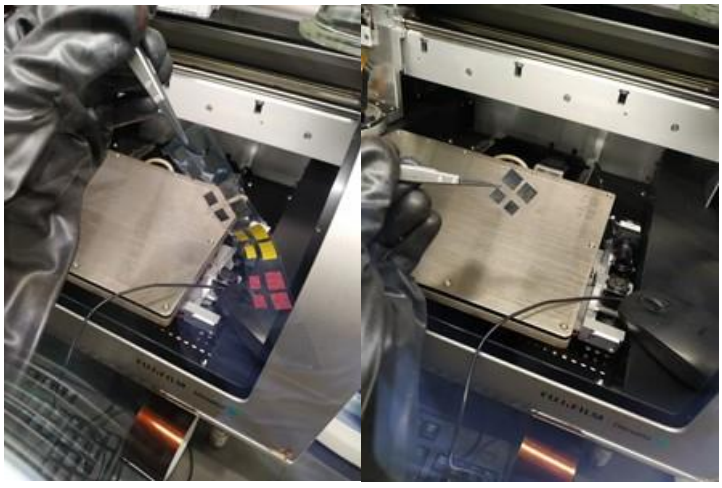

Figure 14. (a) Photograph of different compounds fabricated by ink-jet printing. (b) Detail of the $FASnI_3$ film.

In the first generations of samples ASE was not observed, but the light decoupled at the output edge of the waveguide showed a good PL intensity (together with a lifetime of around 0.5 ns) at room temperature and sufficiently stable with time, as observed in figure 15. It is worth to note that the sample was measured without the need of encapsulation or nitrogen flow with an almost constant PL intensity (figure 15b). Therefore, the optical quality of inkjet printed films is quite promising. In fact, in a subsequent generation of samples, where homogeneity and thickness of the films was improved, ASE was rapidly observed at room temperature in waveguide configuration: see the optical image of the waveguided and PL+ASE spectra of this device in Figure 16.

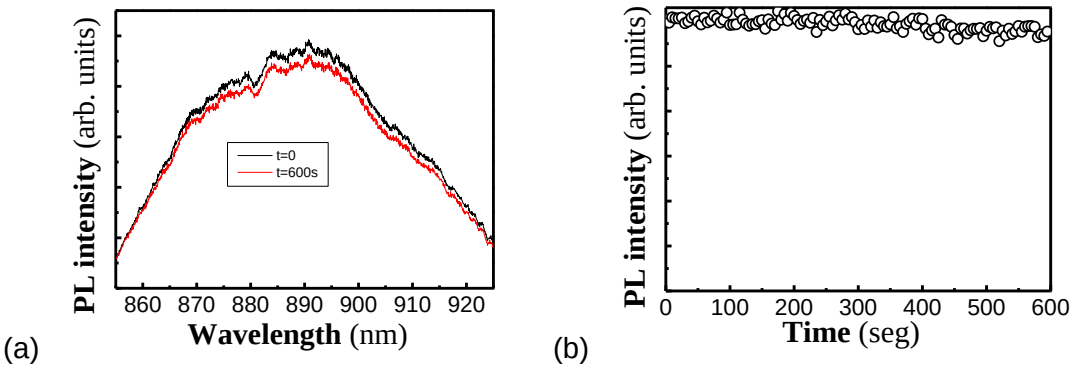

Figure 15. (a) Waveguided PL spectra of $FASnI_3$ film fabricated by ink-jet printing. Black and red colours indicate the time of measurement, 0 and 600 s, respectively. (b) Integrated intensity as a function of the measurement time.

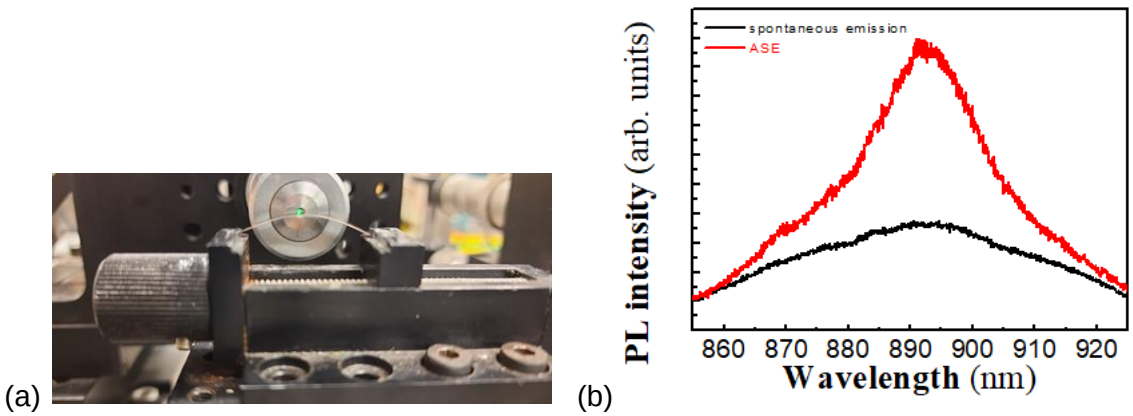

Figure 16. (a) Image of a flexible substrate with the inkjet-printed Sn-perovskite waveguide. (b) Decoupled spectra of waveguided light emitted signal below (spontaneous emission: black continuous line) and above (ASE: red continuous line) the ASE threshold.

4 Deviations from the work plan

None

5 Conclusions & Future directions

To conclude, the $FASnI_3$ film incorporated in a waveguide fabricated on SiO_2/Si rigid and PET flexible substrate by spin coating deposition showed ASE and RL at room T and ambient conditions. The strong electromagnetic field confinement in the waveguide imposes a preferable directionality for emitted light into the optical mode of the waveguide, more important for ASE. Moreover, the WG structure reduce the stimulated emission threshold, down to 0.1 and 1.5 µJ/cm^2 in rigid and flexible substrates, respectively. More importantly, the WG shows a preferable TE ASE and lasing polarization, which is a particular signature for this device not earlier observed for other perovskite-based RL system to the best of our knowledge. The dependence of the threshold and polarization was also studied as a function of the bending radius of the PET substrate, and demonstrates that both the PL, intensity and dichroism can be tuned with the curvature radius. Finally, it is worth mentioning that despite the instability of the Sn-perovskite under ambient conditions, the encapsulation with PMMA together with the measurement under N_2 flows allowed of PL was stable for two hours, which is a remarkable result. The same material fabricated by ink-jet printing also exhibited a high PL intensity and ASE, together with a remarkable stability. Future investigations will include the incorporation of the $FASnI_3$ film on optical cavities to demonstrate lasing (task 5.2) and the incorporation of electrodes to demonstrate a basic integrated photonic circuit (task 5.3).

6 Annex I

Since the first target of task 5.1 is the demonstration of ASE with LFPs, it was necessary to analyze the light-emitting properties of the LFP materials synthesized by the teams of UJI, ETHz, and Avantama. Thus, the photoluminescence (PL) and time-resolved photoluminescence (TRPL) of the different materials (see the list in Table I) were analysed by holding the samples on a cold finger of a closed-cycle He cryostat cooled to 20 K. These experimental conditions allow us to analyse the PL spectra and kinetics without the influence of nonradiative recombination channels (i.e. deep traps or Auger recombination) and without degrading the samples by ambient conditions. The PL and TRPL were measured in backscattering geometry by pumping the LFPs with a Ti:sapphire mode-locked laser at a wavelength of 405 nm doubled by a BBO crystal. The PL signal was dispersed by a double 0.3 m focal length grating spectrograph and detected with an Andor Newton 970 EMCCD camera (PL. TRPL signal was measured with the laser in pulsed operation (200 fs, 76 MHz), and collecting the emitted signal by a Si avalanche photodiode connected to a time-correlated single-photon counting device.

The LFP materials included: Cs_2SnI_6, Cs_3Bi2I_9, Ag_2Bi_{I5} and Ag_3BiI_6 nanocrystals (NC); Cs_2SnI_6, Cs_2SnBr_6, $Cs_2NaInCl_6$, Cs_2InBr_5, Cs_2KInCl_6 powders of bulk materials; and FASnI3 (bulk) polycrystalline thin films. All samples were deposited on glass by deep (nanocrystals and powder) and spin coating techniques (thin films). The NCs and powders, however, present either very low PL intensities or very long lifetime (µs) to conclude that they are suitable materials for optical amplification. Nevertheless, the strong PL emission together with the ~ 1 ns lifetime of the $FASnI_3$ thin films suggests that this material presents the required quantum yield of emission and photophysical properties for stimulated emission. Therefore, we concentrated our investigations on the analysis of these polycrystalline films, as it is described in the present report.

Material	**Form**	**Team-producer (method)**	**Emission (how strong) ***	**Lifetime ***	**ASE****
Cs_2SnI_6 (Sn^{4+})	NCs (8-14 nm)	Avantama (ball-milling)	736 nm (very weak)	0.75 ns	no
Cs_2SnI_6 (Sn^{4+})	Bulk (powder)	UJI (chemical synthesis)	900-1100 (weak)	0.36 ns	no
Cs_2SnBr_6 (Sn^{4+})	Bulk (powder)	UJI (chemical synthesis)	625 nm (PLQY=30-40%)	2.6 ns	no
$FASnI_3$ (Sn^{2+})	Bulk (film)	UJI (spin coating)	890-930 nm (strong)	0.45 ns	yes
$Cs_3Bi_2I_9$	NCs (8-10 nm)	UVEG (laser ablation in liquid)	500-550 nm (weak)	0.5 ns	no
$Cs_2NaInCl_6$	Bulk (powder)	ETHz	620 nm (strong)	~ 1 µs	no
Cs_2InBr_5	Bulk (powder)	ETHz	700 nm (strong)	~ 1 µs	no
Cs_2KInCl_6	Bulk (powder)	ETHz	550 nm (srong)	~ 1 µs	no
Ag_2BiI_5, Ag_3BiI_6	NCs	Avantama (ball-milling)	750 nm (moderate)	~ 1 ns + 200 ns	no